International Journal of Hydrogen Energy 95 (2024) 1299–1315

Contents lists available at ScienceDirect

International Journal of Hydrogen Energy

journal homepage: www.elsevier.com/locate/he

Experimental investigation on the effect of channel geometry on performance heterogeneity in hydrogen PEM fuel cell

Delio Casadei [a,*], Francesco Verducci [a], Amedeo Grimaldi [a], Diego Croci [b], Alessandro Palmieri [b], Roberto Bianchi [b], Gianmario Picciotti [b], Andrea Casalegno [a], Andrea Baricci [a]

[a] Politecnico di Milano, Energy Department, Via Lambruschini 4A, 20156, Milano, Italy
[b] Eldor Corporation S.p.A., Via Don Paolo Berra 18, 22030, Orsenigo, Italy

ARTICLE INFO

Handling Editor: Ibrahim Dincer

Keywords:
Polymer electrolyte membrane fuel cell
Flow field
Heterogeneity
Channel
Electrical contact
Transport resistance

ABSTRACT

Straight parallel graphite-based flow fields are experimentally assessed to evaluate the effect of geometrical parameters on the performance of polymer electrolyte membrane fuel cell. A 1+1D fuel cell model is exploited to evaluate the local operating conditions occurring along various positions of the flow field channel for different load requirements. The estimated operating conditions are implemented in a zero-gradient hardware to perform a broad experimental campaign, conducting tests under controlled and uniform operating conditions. The achieved experimental results depict the impact of the flow field geometry along different positions of the flow field channel under real operating conditions, identifying the individual contributions of the geometric parameters on water transport, oxygen transport and electrical resistance. The proposed methodology provides detailed information on the local operation of a large-area bipolar plate using a small-area sample, demonstrating the effect of rib and channel geometrical parameters on real-world operation of a PEMFC.

1. Introduction

Polymer electrolyte membrane fuel cells (PEMFCs) are electrochemical devices that directly convert hydrogen into electric power with high efficiency, in a scenario where hydrogen is becoming increasingly important [1] and are thus a potential candidate to foster the diffusion of hydrogen technologies for mobility and stationary applications [2–4]. The development of PEMFCs achieved a crucial point in the last years when several targets were reached (efficiency, fast start-up and also durability for automotive applications), but challenges remain in meeting cost and durability targets for high power applications, such as heavy-duty transport or stationary applications combined with renewable energy production [5,6]. Material development is focusing mostly on the core components of PEMFC, in particular the membrane electrode assembly and the bipolar plate, for the latter the US Department of Energy predict that the cost will be 6% of the total stack cost with a volume production of 100,000 systems per year [7].

Bipolar plate is a key component of the PEMFC stack that separates hydrogen, air and the cooling fluid, while also ensuring efficient electrical contact between the cells in the stack, minimizing the ohmic loss [8]. Mechanical and chemical stability are necessary requirements to avoid contamination of the membrane electrode assembly, leading to the study of different materials in the past. Metal bipolar plates are commonly adopted in automotive applications [9] due to their ease of mass production, cost effectiveness and high mechanical strength [10,11]. However, they exhibit low corrosion resistance and, to overcome this issue, it is necessary the addition of protective coating which increases component costs [12,13]. Carbon-based bipolar plates are prevalently used in heavy-duty transport and stationary applications, where their larger volume is not a significant concern, while they ensure the achieving of high durability targets because of their superior corrosion resistance [14]. Both metallic and carbon-based bipolar plates share the design of the gas channel distribution geometry. Hydrogen and air flow in the stack through manifolds, feeding each cell uniformly. Channels within each bipolar plate are manufactured to distribute reactants evenly over the cell surface. The design of the gas channels is of primary importance to deal with the heterogeneity of local operating conditions and to ensure high efficiency and durability. Different works have demonstrated that gas channels significantly affect pressure drops [15], water management [16,17], oxygen concentration [18,19] and that the heterogeneous conditions can lead to local degradation issues [20]. Studies conducted through the use of computational fluid dynamics (CFD) simulations investigate the impact of various factors on

* Corresponding author.
E-mail address: delio.casadei@polimi.it (D. Casadei).

https://doi.org/10.1016/j.ijhydene.2024.08.515
Received 9 April 2024; Received in revised form 29 August 2024; Accepted 31 August 2024
Available online 19 September 2024
0360-3199/© 2024 The Authors. Published by Elsevier Ltd on behalf of Hydrogen Energy Publications LLC. This is an open access article under the CC BY license (http://creativecommons.org/licenses/by/4.0/).

List of acronyms and abbreviations

CCM	Catalyst coated membrane
CFD	Computational fluid dynamics
CV	Cyclic voltammetry
ECSA	Electrochemically active surface area
EIS	Electrochemical impedance spectroscopy
F	Faraday's constant
GDL	Gas diffusion layer
HFR	High frequency resistance
HP	High power
i_{lim}	Limiting current
LP	Low power
LSV	Linear sweep voltammetry
MEA	Membrane electrode assembly
ORR	Oxygen reduction reaction
p	Gas total pressure
PEM	Polymer electrolyte membrane
PEMFC	Polymer electrolyte membrane fuel cell
p_w	Water vapor pressure
R	Universal gas constant
R/C	Rib-to-channel thickness ratio
RH	Relative humidity
R_T	Oxygen transport resistance
SEM	Scanning electron microscopy
T	Temperature
x_{O2}^{dry}	Oxygen dry mole fraction

performance and operating conditions, including the number of channels [21], channel height [22], channel length [23], channel cross-section [15,24], rib and channel dimensions [25–27] and the introduction of baffles [28–32] and sub-channels [33]. In literature, some academic research groups experimentally investigate the effect of channel and rib geometry [34,35] as well as the electrical contact between the bipolar plate and gas diffusion layer (GDL) [36,37]. However, experimental assessment of flow field geometries is not deeply investigated in the literature while the same topic was investigated by means of CFD simulations [38–40]. This work aims to provide a comprehensive analysis of geometric parameters on performance to fill this gap and, to the best of the authors' knowledge, it represents the first experimental methodology which can be applied to locally optimize the geometry of a full-scale flow field.

In this work an experimental analysis is carried out to evaluate the effect of the geometrical features of the channels at the air side on local membrane electrode assembly (MEA) performance. Geometrical features are investigated with reference to a high-performance flow field geometry that is consistent with state-of-the art geometries adopted for automotive applications [41]. An innovative methodology is applied in this work that exploits the use of a zero-gradient hardware presented by the authors in a previous publication [42]. The zero-gradient hardware has a specific design that minimizes heterogeneity of the operating conditions across the sample area, ensuring uniform pressure, gas composition and temperature. This testing tool is adopted to evaluate the cell performance under conditions consistent with real-world scenarios. A 1+1D model validated in a previous research is exploited [43] to assess local conditions along the channel, such as oxygen mole fraction, temperature, pressure relative humidity and water management. The proposed methodology is a powerful and innovative tool that, through experimental characterization with small-scale hardware and a simple setup, provides insights into the local performance of large-scale flow fields with various geometries under real-world operating conditions.

2. Experimental methodology

2.1. Membrane electrode assembly

Commercial materials were adopted in the experimental campaign to minimize uncertainties related to in-house production of the tested MEAs. Each MEA evaluated in this study consists of a commercial catalyst coated membrane (CCM) with a 15 μm membrane thickness, platinum loading of 0.4 mg cm^{-2} at the cathode side and 0.1 mg cm^{-2} at the anode side. The commercial GDLs employed in this study are Freudenberg H14CX483. The specific characteristics of the CCM and GDL are detailed in Table 1.

Table 1
Characteristics of the tested MEAs. The features are declared by the manufacturer or were obtained through scanning electron microscopy (SEM) images.

Characteristic	Unit	
Cathode catalytic loading	mg cm^{-2}	0.4
Anode catalytic loading	mg cm^{-2}	0.1
Membrane thickness	μm	15
Cathode catalyst layer thickness	μm	12
Anode catalyst layer thickness	μm	4
GDL thickness @ 0.025 MPa	μm	180
GDL thickness @ 1 MPa	μm	140
Through-plane electrical resistance @ 1 MPa	mΩ cm^2	6
In-plane electrical resistance	Ω	1.1
Through-plane air permeability acc. to Gurley	s	1
In-plane air permeability @ 1 MPa	$μm^2$	1.2

Rigid PTFE gaskets were used to align the MEA, define the active area and ensure 80% mechanical compression of the MEAs.

2.2. Testing hardware and flow fields

A zero-gradient testing hardware was used to carry out the experimental campaign. The tool was specifically developed and it is described in Ref. [42] and a 3D drawing is reported in Fig. 1a. The hardware is characterized by an active area of 10 cm^2 and by co-flow straight-parallel flow field channels on both the anode and cathode sides. Having a sample with lower active area compared to typical applications (approximately 1:10), a high flow rate is allowed (10:1) having compatible gas velocity in the gas channels that leads to good representativeness of the results.

Cathode flow field plates were produced on purpose with various geometries to assess the impact of geometric features on fuel cell performance. The flow fields assessed in this work are outlined in Fig. 1b and their geometric parameters are detailed in Table 2. Specifically, 5 cathode flow fields were fabricated to investigate the influence of rib thickness, channel thickness and channel depth on PEMFC performance. Starting from the base-case FF-A: FF-B maintains the same rib-to-channel thickness ratio (R/C) but features higher rib and channel thickness; FF-C presents the same rib thickness as FF-B but with a higher R/C; FF-D shares rib thickness of FF-A while having a comparable R/C to FF-C; FF-E is similar to FF-B but shows an increased channel depth to

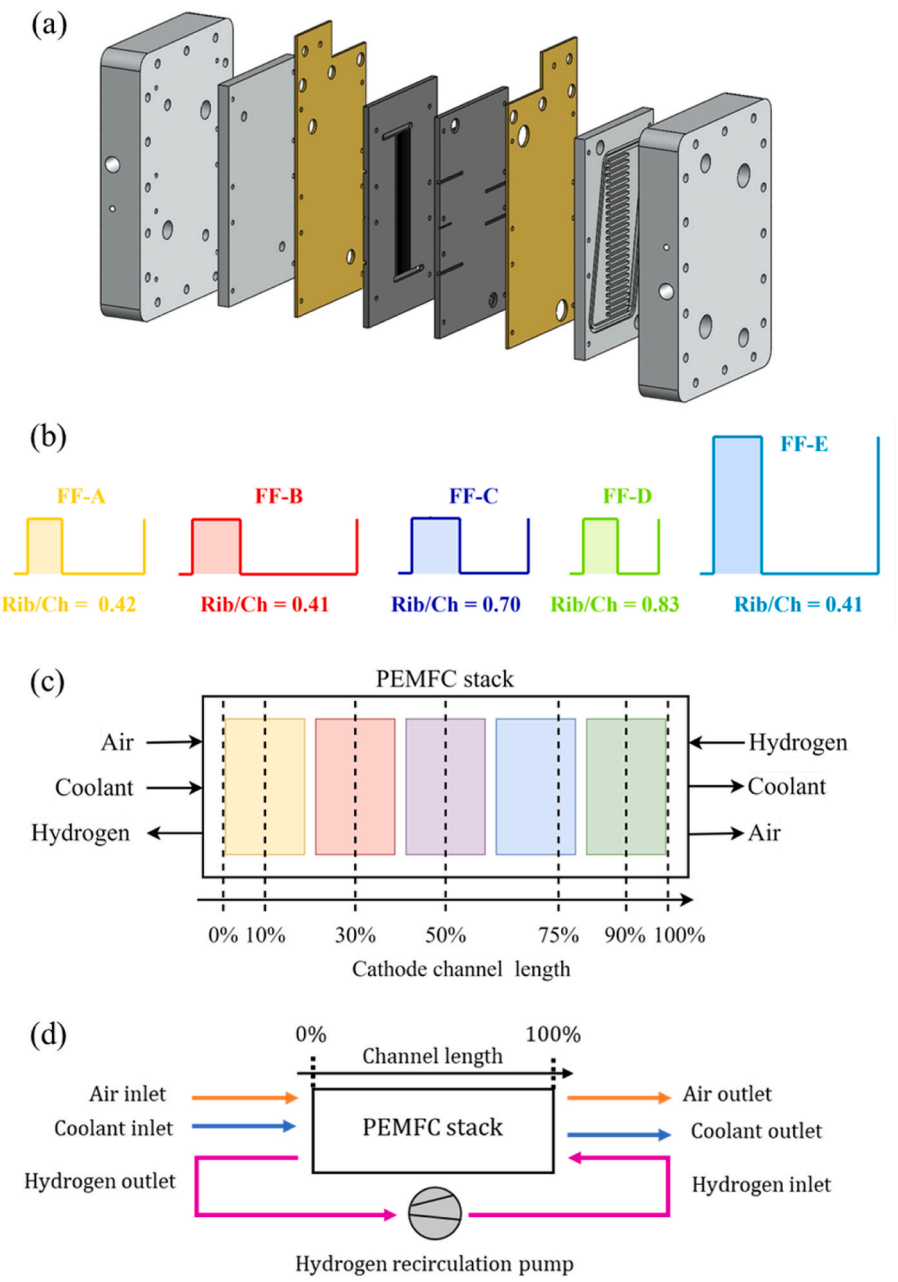

Fig. 1. (a) 3D drawing of the zero-gradient hardware. (b) Scheme of the flow field geometric parameters assessed to investigate the effect of the rib thickness, channel thickness and channel depth. (c) Outline of the positions of the cathode channel length at which operating conditions are evaluated. (d) Scheme of the 1+1D PEMFC model adopted to assess the local operating conditions investigated in the experimental campaign.

Table 2
Geometric parameters of the tested cathode flow field plates.

Name	Rib thickness mm	Channel thickness mm	Channel depth mm	Rib-to-channel thickness ratio
FF-A	0.25	0.60	0.40	0.417
FF-B	0.35	0.85	0.40	0.412
FF-C	0.35	0.50	0.40	0.700
FF-D	0.25	0.30	0.40	0.833
FF-E	0.35	0.85	1.00	0.412

assess the effect of this specific parameter.

The anodic flow field plate remains identical throughout the entire experimental campaign. This decision derives from the understanding that changes on the anode side result in performance variations that are minor compared to the substantial impact of changes in the cathode flow field geometry [44]. The anode flow field utilized in the experimental campaign is characterized by a rib thickness of 0.55 mm, a channel thickness of 0.30 mm and a channel depth of 0.30 mm.

2.3. PEM fuel cell test protocols

The experimental tests were carried out in a testing station which was already described in previous works [20,45]. The protocols for characterization are here described.

Each MEA undergoes an identical conditioning procedure immediately after the assembly. The sample temperature is set at 80 °C, hydrogen and air are supplied under fully humidified conditions at ambient pressure with mass flow rates consistently maintained at 750 ml/min for hydrogen and 3750 ml/min for air. The voltage is varied

between 0.6 V and 0.2 V, with each point lasting 60 s. The procedure is iterated to thoroughly activate the sample that takes about 3 h.

Cyclic voltammetry (CV) tests are conducted at 30 °C, using fully humidified H_2–N_2 gas reactants, with voltage ranging between 0.09 V and 0.6 V to determine the electrochemically active surface area (ECSA).

Linear sweep voltammetry (LSV) measurements are carried out under fully humidified H_2–N_2 gas reactants at ambient pressure and temperature to assess hydrogen crossover and short-circuit resistance. Additionally, LSV tests are conducted at 80 °C and at cathode inlet pressure of 150 kPa, 250 kPa and 350 kPa to evaluate hydrogen crossover values which are used for subsequent corrections in mass transport measurements.

Each sample is experimentally characterized with polarization curves, electrochemical impedance spectroscopy (EIS) and limiting current measurements. Polarization curves are performed under reference conditions, as detailed in Table 3. Measurements are carried out in galvanostatic mode, each data point is maintained for 180 s, only the final 120 s of each point are recorded to ensure assessment under stable conditions. Additionally, polarization curves are performed using the same experimental procedures under operating conditions obtained through model simulations in section 2.4. Polarization curves exhibit an experimental error dependent on current density and operating conditions, not exceeding 4 mV. Error bars are not included in the figures to prevent increased complexity and reduced readability of the figures themselves. For every polarization curve, EIS measurement are conducted at 0.6 A cm^{-2}, 1 A cm^{-2}, 2 A cm^{-2} and 3 A cm^{-2} across a frequency range from 10 kHz to 0.1 Hz, covering 50 different frequencies.

Limiting current measurements are carried out relying on the experimental procedures proposed by Baker et al. [46] and by Greszler et al. [47]. The cell temperature is maintained at 80 °C, with both the anode and the cathode sides supplied by fully humidified gas flow rates. Measurements are conducted under oxygen concentrations of 1%, 2% and 3% on a dry basis at the cathode inlet section. This procedure is repeated for cathode inlet pressure of 150 kPa, 250 kPa and 350 kPa, with the anode inlet pressure set 20 kPa higher. Current density values are recorded at 0.3 V, 0.2 V and 0.1 V to ensure the achieving of limiting current conditions. Under limiting current conditions, the oxygen concentration at the cathode catalyst layer approaches zero and the oxygen transport resistance R_T can computed as [46]:

$$R_T = \frac{4F\, x_{O2}^{dry}}{i_{lim}} \frac{p - p_w}{RT}$$

where F is the Faraday constant, i_{lim} is the measured limiting current, x_{O2}^{dry} is the dry mole fraction of oxygen, p is the gas total pressure, p_w is the water vapor pressure, R is the universal gas constant, T is the cell temperature. The oxygen transport resistance can be divided into a pressure-dependent component, associated with intermolecular gas diffusion thought flow field channel and the larger pores of the GDL, and a pressure-independent component, which is related to Knudsen diffusion occurring in the smaller pores of the microporous layer and catalyst layer [46,48].

2.4. Characterization procedures under real operating conditions

Each sample undergoes a further analysis under operating conditions representative of real-world applications. The operating conditions occurring within a full-scale cell are assessed at various positions along the length of the cathode flow field channel, as depicted in Fig. 1c. In particular, positions at 0%, 10%, 30%, 50%, 75% 90% and 100% of the cathode channel length are considered. These conditions are used as basis for carrying out the testing campaign in zero-gradient hardware, reproducing the performance locally achieved along the channel. To identify these conditions, a 1+1D transient, multiphase and non-isothermal PEM fuel cell model is employed [43]. Coupling a 1D through-the-membrane model with a 1D along-the-channel model, it is possible to assess specific operating parameters across the stack at different positions of the cathode flow field channel length. The model, whose structure is schematized in Fig. 1d, is implemented into Matlab®-Simulink environment adopting a counterflow configuration, with the coolant flow running parallelly to the air stream, along with anodic recirculation and straight-parallel flow field channels.

Based on system requirements [20], some key parameters (Table 4) such as cathode and anode stoichiometries, inlet relative humidity of the cathodic stream and inlet coolant temperature are fixed and provided as inputs to the model. Two distinct operating modes are analysed: the former, indicated as low power (LP), is representative of low engine load conditions and is characterized by a cell voltage of 0.75 V; the latter, indicated as high power (HP), reproduces high load requirements and is characterized by a cell voltage of 0.65 V. The PEMFC model is used solely as a tool to identify how operating conditions vary along the channel length and the validation of the model on experimental data is beyond the scope of this paper. Moreover, it is important to note that the 1+1D model was calibrated on a material with well-known properties, although they were made with a different catalyst with respect to the one analysed in this work, presenting different kinetics and oxygen/-proton transport properties. This may explain the possible discrepancies between model simulations and the experimental data presented in the following which, however, since these differences do not greatly affect water balance and relative humidity they do not significantly influence the methodology and main results presented in this paper.

3. Results and discussion

3.1. Assessment of real-world local operating conditions

The main results of this modelling analysis are reported in Fig. 2 and

Table 4
Model boundary conditions for the low power (LP) and high power (HP) operating modes.

Operating parameters	Low power (LP)	High power (HP)
Cell voltage [V]	0.75	0.65
Cathode stoichiometry [−]	1.6	1.6
Anode stoichiometry [−]	1.4	1.4
Inlet cathode RH [%]	30	30
Inlet anode RH [%]	Controlled by anodic recirculation	Controlled by anodic recirculation
Inlet cathode p [bar]	1.4	2.8
Inlet anode p [bar]	1.9	3
Inlet x_{O2}^{dry} [−]	0.209	0.209
Inlet coolant T [°C]	68	85
Outlet coolant T [°C]	73	90

Table 3
Polarization curves operating conditions used for sample characterization under reference conditions. Stoichiometries for cathode and anode are respectively 10/8 under air conditions and 48/8 under oxygen conditions.

Name	T cell	Dew point cathode	Dew point anode	RH cathode	RH anode	p cathode inlet	p anode inlet	x_{O2}^{dry}
	°C	°C	°C	%	%	$kPa_{,abs}$	$kPa_{,abs}$	%
Air-Ref	80	80	80	100	100	230	250	20.9
O2-Ref	80	80	80	100	100	230	250	100
O2 RH30%-Ref	80	45	45	30	30	230	250	100

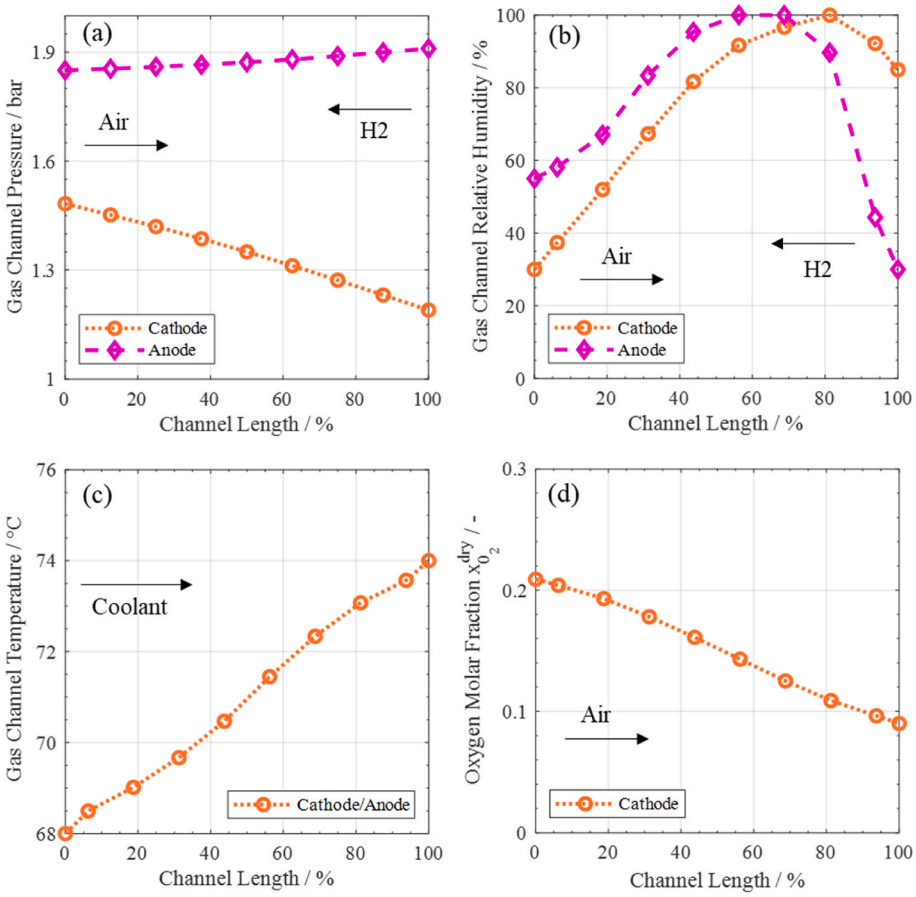

Fig. 2. Results predicted by the 1+1D PEMFC model for the LP operating conditions: (a) gas channel pressure, (b) gas channel relative humidity, (c) gas channel temperature and (d) oxygen mole fraction at different positions of the cathode flow field channel length.

Fig. 3 for LP and HP operating modes respectively. The channel length coordinate is consistently defined with respect to the air feed. Hydrogen is counter-flow while liquid cooling is co-flow with the air flow.

Under LP operation, gas pressure (Fig. 2a) decreases linearly from the channel inlet to the outlet because of pressure drops in the channels. In particular, due to the larger air mass flow rate, and hence higher velocity, the cathode side exhibits pressure drops approximately four times greater than those observed in the anode channel. Examining the evolution of gas composition along the channel in the LP operating point (Fig. 2b), because of the water production along the channel a progressive increase in the relative humidity of the air stream is observed up to 80% of the channel length, where a fully humidified condition is achieved. Towards the end of the air channel (60%–100% length), the net water flux across the membrane reverses direction, flowing from cathode side to anode side [49]. This phenomenon is a consequence of the counterflow configuration and determines a reduction in the relative humidity of the cathode channel from 80% to 100% of channel length, accompanied by an increase in the relative humidity of the hydrogen stream, which reaches its maximum value around the 60% of the channel length. Temperature (Fig. 2c) increases linearly from the air inlet (0%) to the outlet (100%) parallel to the direction of the coolant flow, due to heat release from oxygen reduction reaction (ORR) and overpotentials associated to ohmic phenomena and electrochemical reactions. Oxygen mole fraction is reported on a dry basis in Fig. 2d, it shows a decreasing trend consistent with progressive oxygen consumption because of the ORR. Considering all these aspects, model predictions suggests that the maximum cell power output occurs around 55–60% of the channel length, situated in the middle region of the cell. Additional details about the local operating conditions assessed through the modelling analysis are reported in Table 5, where the values at different channel lengths are obtained through a linear interpolation of the data derived from numerical simulations and shown in Fig. 2.

The HP operation, as it can be observed in Fig. 3, is characterized by more severe operating conditions. Indeed, the higher power requirements typical of the HP operating mode necessitate larger air and hydrogen mass flow rates. This determines elevated flow velocities in both the anodic and cathodic channels, leading to significant pressure drops (Fig. 3a). In particular, pressure drops at cathode side are approximately twice those predicted by the model in the LP mode, while those estimated at the anode side are four times larger. The higher cell temperature enhances water removal and evaporation in the gas channels, as already observed for the higher flow velocity, thus determining a lower maximum relative humidity (Fig. 3b). Fully humidified conditions are not achieved in either the cathodic or anodic sides. Due to the counterflow configuration, the relative humidity at anode side increases from the air outlet to the air inlet, reaching its maximum at around 20% of the cathode channel length. Then, moving further towards the cathode inlet, a net water flux from the anode to the cathode side leads to a slight decrease in the relative humidity of hydrogen stream, reaching a value of 85% at the anode channel outlet. It is worth noting that, with respect to LP, the HP operation leads to a more uniform water distribution, which should be taken into account in flow field design. The stricter operating conditions of the HP mode are also highlighted by the temperature profile (Fig. 3c), which increases from 85 °C at the cathode inlet (0%) to approximately 90 °C at stack outlet (100%). Once again, oxygen is progressively consumed along the channel length (Fig. 3d), although it decreases more rapidly with respect to LP operation due to the higher load required to the cell. Consequently, the maximum power output predicted by the model shifts closer to the cathode inlet, at around the 30% of flow field length. Further details about the local

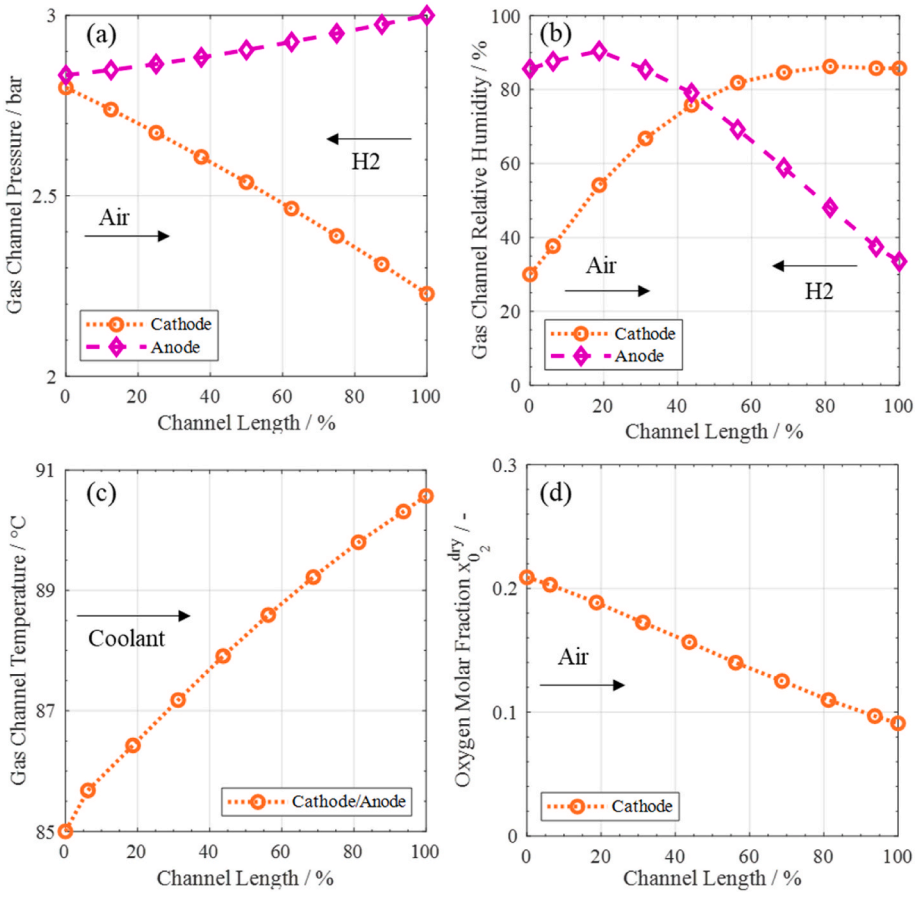

Fig. 3. Results predicted by the 1+1D PEMFC model for the HP operating conditions: (a) gas channel pressure, (b) gas channel relative humidity, (c) gas channel temperature and (d) oxygen mole fraction at different positions of the cathode flow field channel length.

Table 5
Polarization curves operating conditions for different cathode channel length percentages used for sample characterization under low power operating conditions. Stoichiometries for cathode and anode are respectively 10/8.

Name	T cell	Dew point cathode	Dew point anode	RH cathode	RH anode	Cathode inlet pressure	Anode inlet pressure	x_{O2}^{dry}
	°C	°C	°C	%	%	bar_{abs}	bar_{abs}	%
LP0%	68	43	55	30	55	1.40	1.80	20.9
LP10%	69	49	58	40	60	1.38	1.80	19.9
LP30%	69	58	64	60	80	1.34	1.83	18.5
LP50%	70	65	70	80	100	1.30	1.85	16.0
LP75%	72	72	72	100	100	1.25	1.88	12.0
LP90%	72	71	60.5	95	60	1.22	1.90	10.0
LP100%	73	69	47	85	30	1.20	1.90	9.0

Table 6
Polarization curves operating conditions for different cathode channel length percentages used for sample characterization under high power operating conditions. Stoichiometries for cathode and anode are respectively 10/8.

Name	T cell	Dew point cathode	Dew point anode	RH cathode	RH anode	Cathode inlet pressure	Anode inlet pressure	x_{O2}^{dry}
	°C	°C	°C	%	%	bar_{abs}	bar_{abs}	%
HP0%	85	57	79	30	80	2.80	2.80	20.9
HP10%	86	64	83	40	90	2.76	2.82	19.9
HP30%	87	76	84	65	90	2.68	2.86	17.5
HP50%	88	82	82	80	80	2.60	2.90	15.0
HP75%	89	86	76	90	60	2.50	2.95	12.0
HP90%	89	86	69.5	90	45	2.44	2.98	10.0
HP100%	90	86	68	85	40	2.40	3.00	9.0

operating conditions of the HP mode are reported in Table 6.

3.2. Flow field performance under real operating conditions

According to the model analysis, a set of polarization curves is performed for each tested flow field to evaluate the local performance under real-world operating conditions. The local operating conditions assessed for both LP and HP operations (as described in section 3.1) are reproduced in zero-gradient hardware. This approach enables the evaluation in small-scale configuration of performance occurring across various positions within a full-scale cell. Polarization curves are conducted for each operating condition reported in Table 5 and Table 6, identified as a percentage of the channel length (0%–100%) from the air inlet.

Polarization curves obtained experimentally under LP operating conditions are reported in Fig. 4a. The results obtained at 0% and 10% of cathode channel length represent the air inlet region of the stack, where air is fed at low RH. Under these conditions, performance is mainly limited by ohmic loss due to low membrane and cathode catalyst layer hydration [34]. The middle region of the stack is characterized by a performance improvement with respect to the air inlet. This enhancement is attributed to the water produced through electrochemical reactions and the water flux from the anode to the cathode side, which leads to higher membrane hydration and a consequent reduction in ohmic loss [50]. Moving from the middle region of the stack towards the air outlet, polarization curves are increasingly affected by mass transport loss due to the decrease in oxygen mole fraction [51]. The shaded region in Fig. 4a highlights the range of power densities where LP operation occurs. The voltage values range from 0.7 V to 0.80 V and are mainly affected by the observed phenomena: performance improves from the air inlet to the middle region due to better membrane hydration, while a performance reduction is observed from the middle region to the air outlet because of the progressive reduction of oxygen mole fraction. EIS measurements performed under low power conditions at 1 A cm^{-2}, reported in Fig. 4b, evidence a higher value of high frequency resistance (HFR) at the air inlet, indicating that performance is limited by membrane dehydration issues [52]. Moreover, the increase in the low-frequency arc at the air outlet region demonstrates an increase in the mass transport due to the reduction of oxygen mole fraction [53].

Polarization curves obtained experimentally under HP conditions are reported in Fig. 4c. The performance trend presents some similarities to the behaviour observed under LP conditions, although some differences are notable. The transition from low to high membrane hydration is still evident when comparing the air inlet to the middle region, but its impact on performance is less pronounced compared to LP conditions. This is consistent with increased water production at high current density which counteracts low relative humidity in the gas feed [54]. Within the operating voltage (from 0.6 V to 0.7 V), oxygen transport limitations represent a more significant constrain compared to LP operation. The higher reduction in oxygen mole fraction due to the higher current density leads to a performance reduction even at 50% of the cathode channel length and this influence becomes more pronounced moving towards the air outlet section. EIS measurements carried out under high power conditions at 2 A cm^{-2} are reported in Fig. 4d and similar considerations reported for LP hold. The increase in the low-frequency arc from the air inlet to the air outlet confirms the increase in mass transport

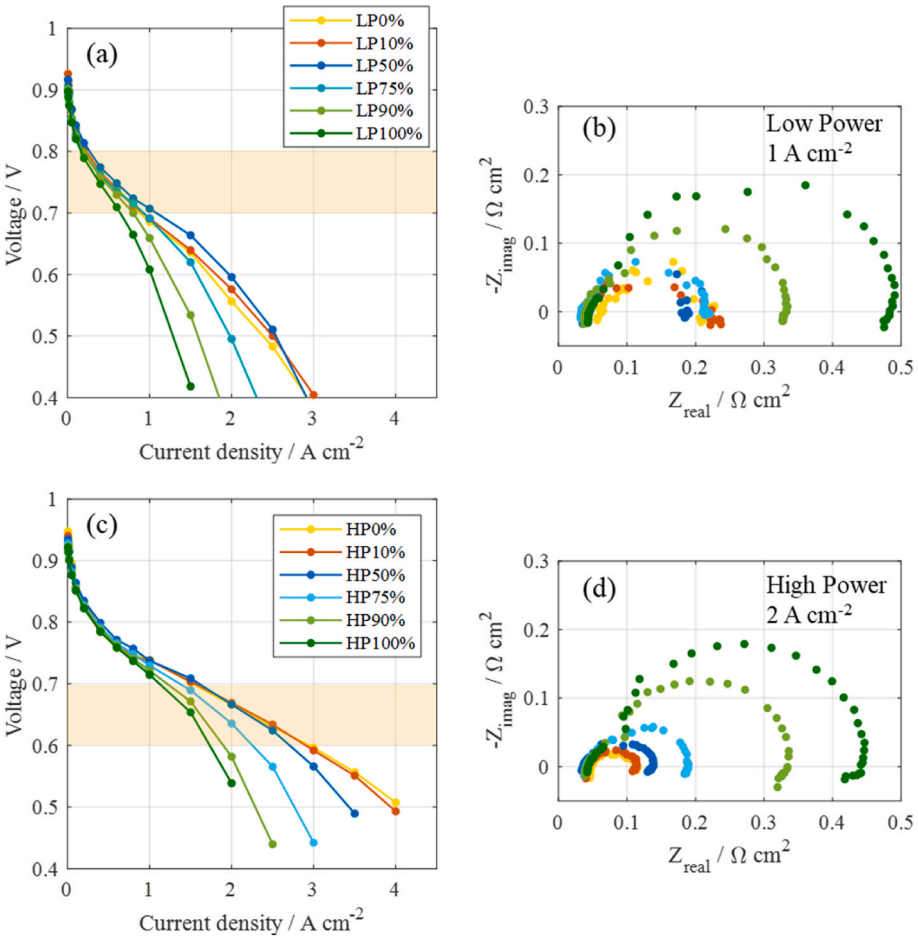

Fig. 4. Polarization curves and EIS measurements carried out under low power and high power operating conditions at different values of the cathode channel length: (a) low power polarization curves, (b) low power EIS at 1 A cm^{-2}, (c) high power polarization curves, (d) high power EIS at 2 A cm^{-2}.

loss, which limits performance in the region close to the air outlet section [53].

A further consideration regarding the analysed operating conditions concerns the heterogeneity in current density among different regions along the channel. The current density spread at 0.75 V in LP conditions is considerably lower compared to HP conditions at 0.65 V. Consequently, high power operation is characterized by heterogeneity among regions, highlighting the need to take into account this aspect in the design of a full-scale flow field.

A comparison under LP and HP conditions between the polarization curves obtained through experiments (Fig. 5a) and model (Fig. 5b) is reported. In both cases it is presented a focus on the operating voltages corresponding to the conditions at which the modes operate. The outcomes demonstrate a good consistency between the performance predicted by the model and the experimental results, even though not strictly adherent. It is anyway confirmed that the local operating conditions assessed with the model and adopted to carry out the experiment accurately represent the operating conditions occurring locally within the stack.

3.3. *Effect of rib-to-channel thickness ratio and of rib thickness*

This section presents a comparison of experimental results obtained from cathode flow field plates labelled as FF-A, FF-B, FF-C and FF-D in Table 2. These samples are characterized by identical channel depth, while the rib thickness and channel thickness vary. A scheme of the geometric parameters of these flow fields is reported in Fig. 1b.

The performance of the flow fields is assessed through characterization under real-world HP and LP operating conditions and polarization curves are reported in Fig. 6, reproducing the local operating conditions occurring at positions 0%-10%-50%-75%-90%–100% along the cathode channel length. In the region close to the air inlet, as shown in Fig. 6a and Fig. 6b, the flow fields labelled as FF-C and FF-D outperform FF-A and FF-B. The distinguishing feature affecting the performance under these conditions is the contact area between the rib and the GDL, which is directly related to the electrical contact resistance between them [8,55]. FF-C and FF-D are characterized by a higher rib-to-channel thickness ratio compared to FF-A and FF-B (as reported in Table 2), resulting in a larger electrical contact. At the same time, high contact area between rib and GDL facilitates the water retention in the cathode catalyst layer and the membrane, improving ion transport resistance as well [56]. In conclusion, in the air inlet region, where ohmic loss was recognized as the primary limiting factor having high oxygen availability but low relative humidity in the cathode gas flow, the electrical and ionic resistances are responsible for the performance difference among the analysed flow fields.

The performance obtained at 50% and 75% of the cathode channel length is reported in Fig. 6c and Fig. 6d respectively. The rib-to-channel thickness ratio plays a key role at low current density values, where polarization curves are primarily limited by ohmic loss. However, mass transport loss leads to a rapid performance drop at medium and high current densities. The assessed flow field geometries show different behaviour in the mass transport region. Indeed, when the rib-to-channel thickness ratio is fixed, flow fields with higher rib thickness present a more rapid voltage drop a high current densities, as it is shown by the performance drop of FF-B and FF-C compared to FF-A and FF-D respectively. A higher rib thickness results in increased liquid water accumulation within the GDL, presumably under the rib [57], increasing the risk of flooding. This phenomenon is particularly pronounced under these operating conditions due to the high relative humidity of the gas flow rates.

The performance achieved in the air outlet region is analysed in Fig. 6e and Fig. 6f. Under these conditions, the reduction in oxygen mole fraction represents the primary limiting factor [58], resulting in a steep voltage drop observed across all assessed flow fields. Flow fields with higher rib-to-channel thickness ratio still present advantages at low current densities, where ohmic loss is the limiting phenomena. However, with increasing current density, a high rib-to-channel thickness ratio becomes detrimental in terms of performance since the reduced area in which channels and GDL face each other leads to an increase in the oxygen transport resistance [32]. Analysing these results it is clear that the limiting phenomena can vary across different positions along the channel length.

For each tested flow field, a power density profile along the channel is obtained and reported in Fig. 7a and Fig. 7b for LP and HP operating conditions respectively. The power density profile is evaluated consistently with the previous analysis. For both LP and HP cases one operating point is obtained for each value of cathode channel length, the outcome of this analysis is reported in Fig. 7 for the flow field plates assessed in this section.

Power density profiles obtained under LP operating conditions, as represented in Fig. 7a, evidence higher performance for flow fields

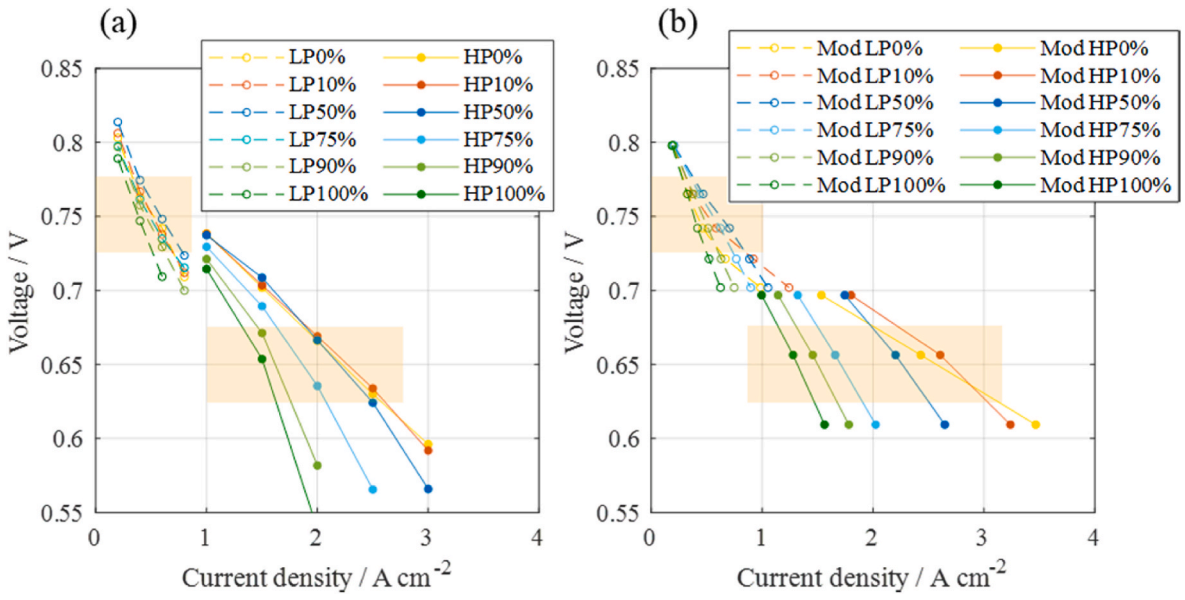

Fig. 5. Comparison under LP and HP conditions between (a) experimental and (b) modelled polarization curves, focusing on the voltage ranges of the corresponding operational states.

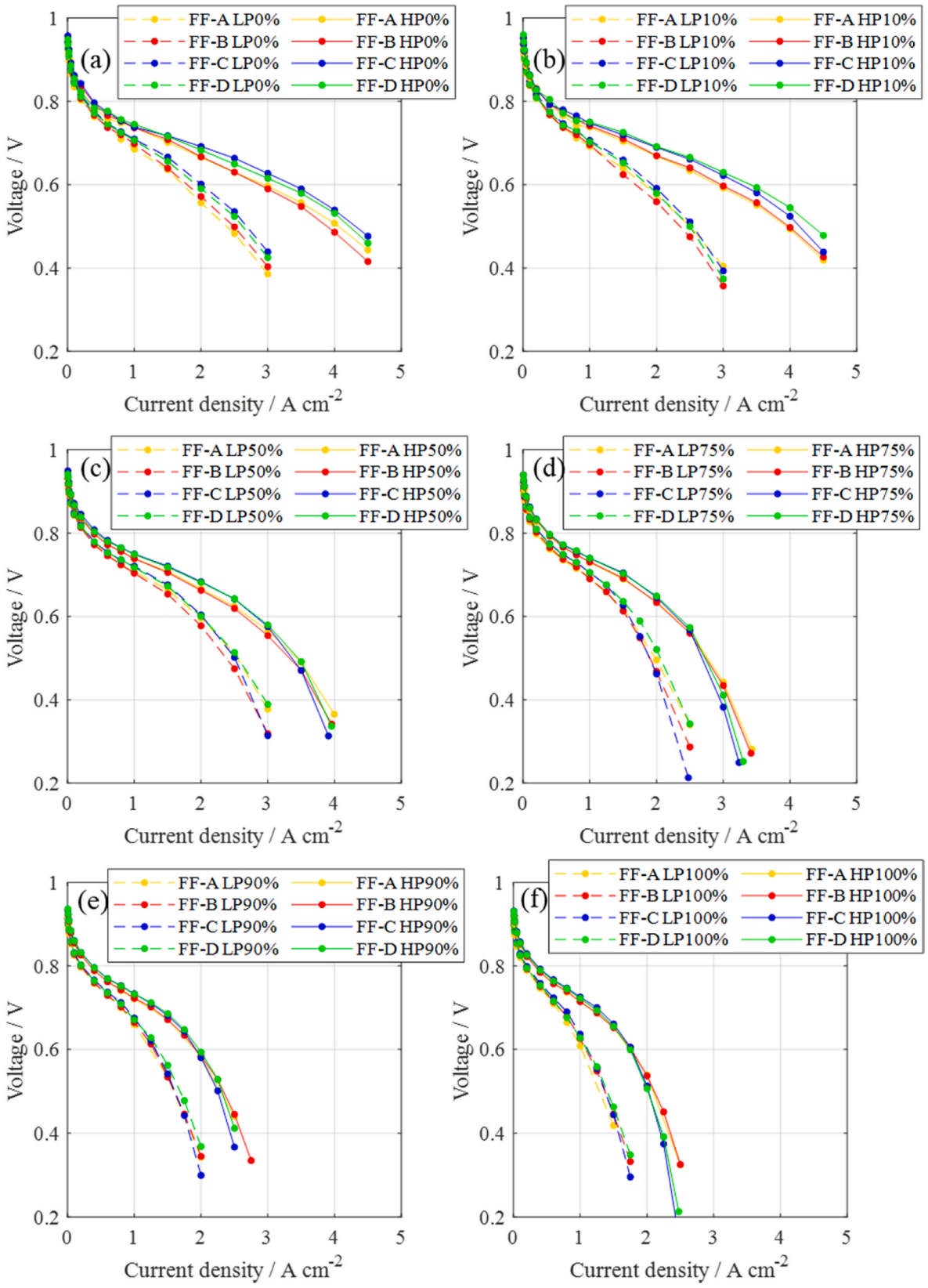

Fig. 6. Polarization curves of four flow field plates characterized by different rib and channel thickness (FF-A, FF-B, FF-C, FF-D) reproducing low power and high power conditions occurring different positions of the cathode channel length: (a) 0%, (b) 10%, (c) 50%, (d) 75%, (e) 90%, (f) 100%.

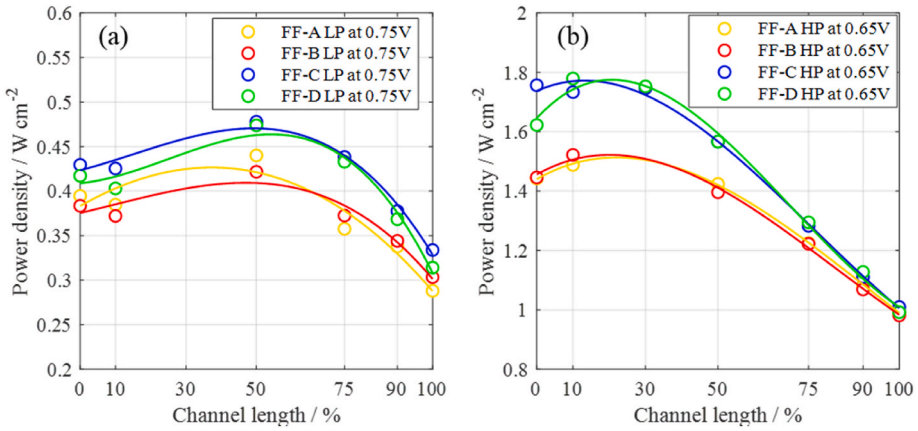

Fig. 7. Power density of four flow field plates characterized by different rib and channel thickness (FF-A, FF-B, FF-C, FF-D) as function of the cathode channel length: (a) low power conditions assessed at 0.75 V, (b) high power conditions assessed at 0.65 V.

labelled as FF-C and FF-D compared to FF-A and FF-B. As confirmed by the previous analysis, at the operating voltage of 0.75 V defined for LP conditions performance is mainly limited by ohmic loss, therefore the flow fields with higher rib-to-channel thickness ratio (FF–C and FF-D) exhibits superior performance [37]. Mass transport loss becomes significant only near the air outlet region due to the lower oxygen mole fraction [59] caused by oxygen consumption along the channel length. Therefore, in the air outlet region the difference among the samples is reduced because of mass transport limitations. It is observed that for samples with comparable rib-to-channel thickness ratio, oxygen transport resistance is higher with greater rib thickness, in accordance with previous findings. A bell-shaped curve is obtained under LP conditions, with a peak around 50% of the cathode channel length, this is due to low cathode gas RH at the air inlet and high mass transport resistance at the air outlet, leading to performance reductions at the air inlet and air outlet region, respectively.

Power density profiles obtained under HP conditions are reported in Fig. 7b. The operating voltage of 0.65 V is lower compared to LP conditions, resulting in a greater impact of mass transport loss since performance is evaluated from polarization curves at higher current densities. In the air inlet region ohmic loss dominates, as already observed under LP conditions, hence the differences among the different flow fields are related to the rib-to-channel thickness ratio. Oxygen transport resistance limits performance in the air outlet region, as seen under LP conditions, but in this case it also affects the central region due to higher current density reached under these conditions, leading to a rapid performance decrease. The power density curve under HP conditions shows an initial performance increase due to the progressive sample hydration, followed by a progressive reduction and homogenization in performance among the different flow fields towards the air outlet region, driven by mass transport loss. As a result, the power density curve peak shifts towards a position closer to the air inlet compared to that observed under LP conditions.

The four flow field geometries assessed in this section are further analysed through polarization curves conducted under pure oxygen conditions, both with fully humidified and 30% relative humidity of gas reactants (O2-Ref and O2 RH30%-Ref conditions reported in Table 3). Polarization curves under oxygen conditions are reported in Fig. 8a. The analysis is insightful as the outcomes are not affected by oxygen mass transport resistance, due to the high availability of the reactant, therefore the main phenomena determining the performance are attributed to ohmic loss. Low and high RH values in the gas feed are used to evaluate the impact of electrical resistance against ionic resistance effects observed for inlet conditions. Samples characterized by a similar rib-to-channel thickness ratio exhibit comparable performances, while an increase in this ratio corresponds to reduced ohmic loss and enhanced performance. The ratio between rib thickness and channel thickness directly influences the contact area between the bipolar plate and the GDL [25]. A higher contact area improves the electrical contact between these two components, resulting in a consequential reduction of the ohmic loss and an overall performance improvement. EIS measurements carried out at 1 A cm^{-2} under oxygen conditions are reported in Fig. 8b and Fig. 8c respectively, with fully humidified (O2-Ref) and 30% relative humidity (O2 RH30%-Ref) of gas reactants. The samples exhibit comparable capacitive features, suggesting consistent ORR kinetic properties, as demonstrated by the charge transport resistance associated to the reported arcs. Differences in EIS among the flow fields arise with the increase of rib-to-channel thickness ratio, resulting in a reduction of the HFR values. Indeed, HFR is a measure of the electrical series including the electrical resistance of the GDLs, MPLs, catalyst layers and bipolar plates as well as the ionic resistance of the membrane [60]. An enhanced electrical contact between bipolar plate and GDL is achieved by increasing the rib-to-channel thickness ratio [37]. The HFR difference between samples with distinct electrical contact area becomes more pronounced moving from fully humidified gas reactants to 30% relative humidity. The increase in HFR under low RH conditions is attributed to membrane dehydration, which leads to a reduction in ionic conductivity [52]. Samples with a higher contact area between bipolar plate and GDL retain more water within the GDL [61], resulting in a reduced HFR under low relative humidity conditions compared to samples with a lower rib-to-channel thickness ratio. It is concluded that positive impact of the rib-to-channel thickness ratio is not solely attributed to electrical contact resistance between GDL and bipolar plate, but also to increased water content in the membrane if low RH is provided in the gas feed.

Fig. 8d depicts polarization curves with air/hydrogen gas reactants (Air-Ref conditions detailed in Table 3). Samples characterized by a higher rib-to-channel thickness ratio exhibits higher performance at mid-current density, a region where ohmic loss is the primary limiting phenomena [59], consistently with observations under pure oxygen conditions. A distinct behaviour arises at current densities exceeding 3.5 A cm^{-2}: when comparing similar values of rib-to-channel thickness ratio, samples characterized by higher rib thickness present liquid water flooding phenomena at high current density [50]. This behaviour is related to the accumulation of liquid water within the GDL in the region under the rib, which is further accentuated with higher rib thickness [62]. In Fig. 8d, polarization curves under air/hydrogen conditions (Air-Ref) are also reported with a correction applied for the value of HFR, which is obtained at 1 A cm^{-2}. The results depict comparable performance up to 3 A cm^{-2}, indicating that the discrepancy in the ohmic region for non-corrected curves is attributable to HFR difference. Meanwhile, at higher current densities, differences in mass transport

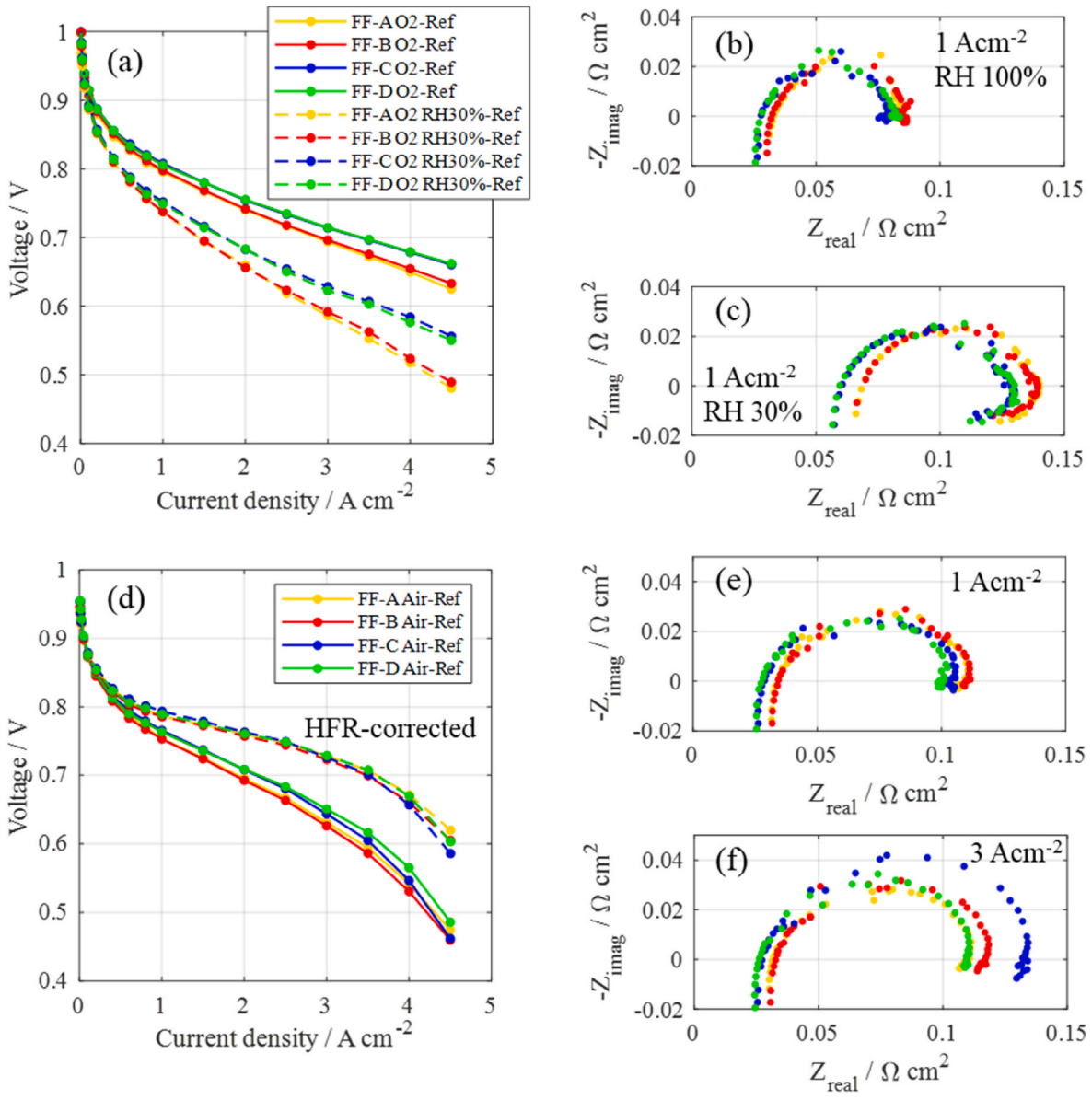

Fig. 8. Performance characterization of four flow field plates with different rib and channel thickness (FF-A, FF-B, FF-C, FF-D). Pure oxygen/hydrogen conditions: (a) fully humidified (O2-Ref) and 30% relative humidity (O2 RH30%-Ref) polarization curves, (b) EIS at 1 A cm^{-2} under fully humified conditions (O2-Ref), (c) EIS at 1 A cm^{-2} at 30% relative humidity (O2 RH30%-Ref). Air/hydrogen fully humidified conditions (Air-Ref): (d) polarization curves and HFR-corrected polarization curves, (e) EIS at 1 A cm^{-2}, (f) EIS at 3 A cm^{-2}.

become evident even for HFR-corrected curves, revealing higher mass transport loss for samples with thicker rib. EIS measurements at 1 A cm^{-2} and at 3 A cm^{-2} under air/hydrogen conditions (Air-Ref) are reported in Fig. 8e and Fig. 8f respectively. At 1 A cm^{-2} the main observable differences among the considered flow fields are represented by the HFR differences related to variations in rib-to-channel thickness ratio. At higher current density, the measured behaviour reveals an increase in the low frequency arc for FF-B compared to FF-A and for FF-C compared to FF-D, confirming the higher oxygen transport resistance associated to the thicker rib [53].

3.4. Effect of channel depth

The impact of channel depth on sample performance is investigated by introducing an additional flow field labelled as FF-E, which maintains the same channel and rib thickness as FF-B but the channel depth is increased to 1 mm. The performance of the two flow fields geometries are compared in this section. Polarization curves under low power and high power conditions are reported at various percentages of the cathode channel length in Fig. 9.

At 10% of the cathode channel length (Fig. 9a), FF-E appears to achieve performance comparable to FF-B across the low and middle current density range. However, FF-E exhibits a current density that is about 60 mA cm^{-2} higher than FF-B under LP at 0.75 V, and about 170 mA cm^{-2} higher under HP conditions at 0.65 V. Under these operating conditions the limiting factor is the low RH at the cathode side [34]. The performance difference between the two geometries is attributed to the lower gas velocity at the cathode side in case of FF-E, which is a consequence of the larger cross sectional area of the gas flow related to the increased channel depth [22]. The lower gas velocity enhances water retention, resulting in higher membrane hydration [21,63].

The variation in membrane hydration under LP and HP conditions at 10% of the cathode channel length is evidenced by the difference in the HFR values depicted in Fig. 9b. Under these conditions, flow field FF-E

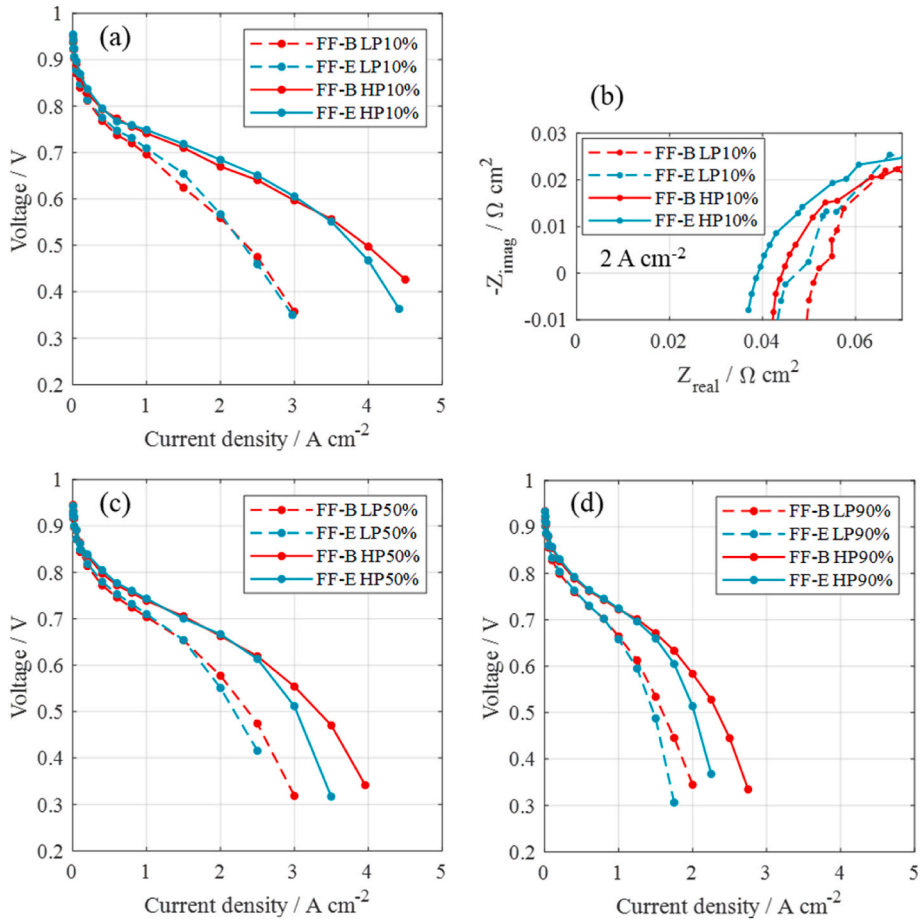

Fig. 9. Experimental measurements carried out under low power and high power operating modes: (a) polarization curves and (b) EIS at 2 A cm^{-2} at 10% of the cathode channel length, (c) polarization curves at 50% of the cathode channel length, (d) polarization curves at 90% of the cathode channel length.

exhibits lower HFR compared to FF-B. This difference is to be attributed to the increased water retention in the membrane, since the rib-to-channel thickness ratio is the same for the two geometries. It is thus attributed to the reduced gas velocity within the cathode channels of FF-E [24,64], which is characterized by a larger channel cross sectional area. The reduction in HFR for FF-E is beneficial for performance and results in lower ohmic loss compared to FF-B [65], as observed in Fig. 9a.

Polarization curves obtained under the operating conditions at 50% of the cathode channel length are reported in Fig. 9c. The two flow fields exhibit comparable performance up to 0.65 V, with noticeable differences only at low cell voltage, not realistic for real-world operation, nevertheless in this condition the sample with shallower channels presents higher performance. In the middle region, where both anode and cathode gas reactants are highly humidified and the membrane is well hydrated, high gas velocity at the air side plays a beneficial role [66]. A higher gas velocity enhances oxygen transport and water removal, resulting in improved performance for FF-B and lower performance for FF-E due to the reduced velocity within the cathode channels [21].

Polarization curves obtained under the operating conditions occurring at 90% of the cathode channel length are depicted in Fig. 9d, these conditions are characterized by high cathode RH and by low oxygen mole fraction. The performance of the two flow fields are comparable up to around 1.25 A cm^{-2}, beyond which the sample with deeper cathode channels exhibits lower performance. Under these conditions, the lower velocity within the cathode channels further negatively impacts the oxygen transport resistance to the electrodes [24], resulting in lower performance for FF-E at high current densities. The difference in oxygen transport is attributed to variations in mass transport convection caused by different flow velocities within the channel. The resulting differences in the laminar boundary layer affect the velocity within the GDL, thereby influencing oxygen transport from the channel to the catalyst active sites.

Power density profiles at different positions of the cathode channel length are derived from low power and high power polarization curves, with the operating voltage fixed at 0.75 V for LP conditions (Fig. 10a) and 0.65 V for HP conditions (Fig. 10b). The results evidence that a deeper channel achieves higher power density at the air inlet and in the central region under LP conditions. This is consistent with the considerations reported before and attributed to the gas velocity. Lower water removal from the MEA and better membrane hydration is achieved for FF-E in all the positions where increasing water retention is positive for performance [15]. However, in the region from the middle of the stack to the air outlet, oxygen transport becomes increasingly important, in particular at higher current densities, as in HP. Under these conditions a deeper channel is detrimental to performance and shallower channels are preferable, consolidating the finding that higher air velocity in the gas channel enhances oxygen transport and reduces the risk of liquid water flooding [27].

Polarization curves of FF-B and FF-E under pure oxygen conditions are reported in Fig. 11a, considering both fully humidified (O2-Ref) and 30% RH (O2 RH30%-Ref) conditions. Under fully humidified conditions, both flow fields geometries present similar results, with slightly higher performance achieved by FF-E, characterized by deeper channels. FF-E maintains higher performance compared to FF-B even under 30% RH of gas reactants and moreover, the voltage difference between them is more pronounced compared to fully humidified conditions. EIS measurements obtained at 1 A cm^{-2} under fully humidified (O2-Ref) and 30% relative humidity of gas reactants (O2 RH30%-Ref) are

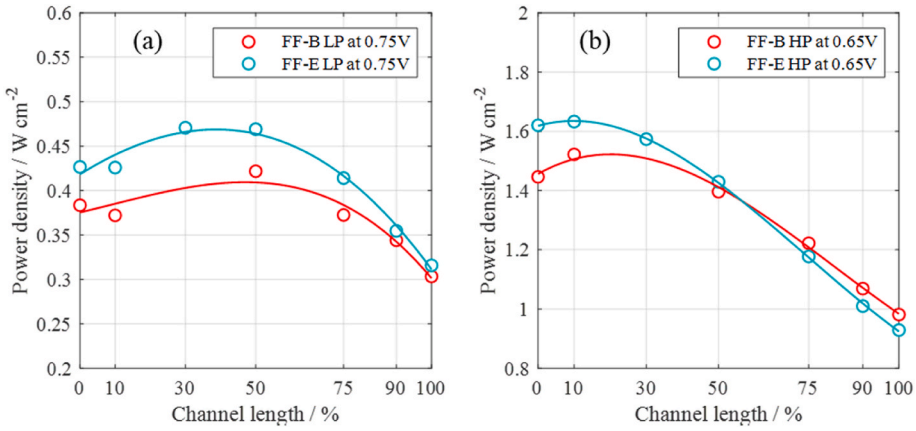

Fig. 10. Power density at various cathode channel lengths under (a) low power conditions and (b) high power conditions assessed at 0.75 V and 0.65 V respectively.

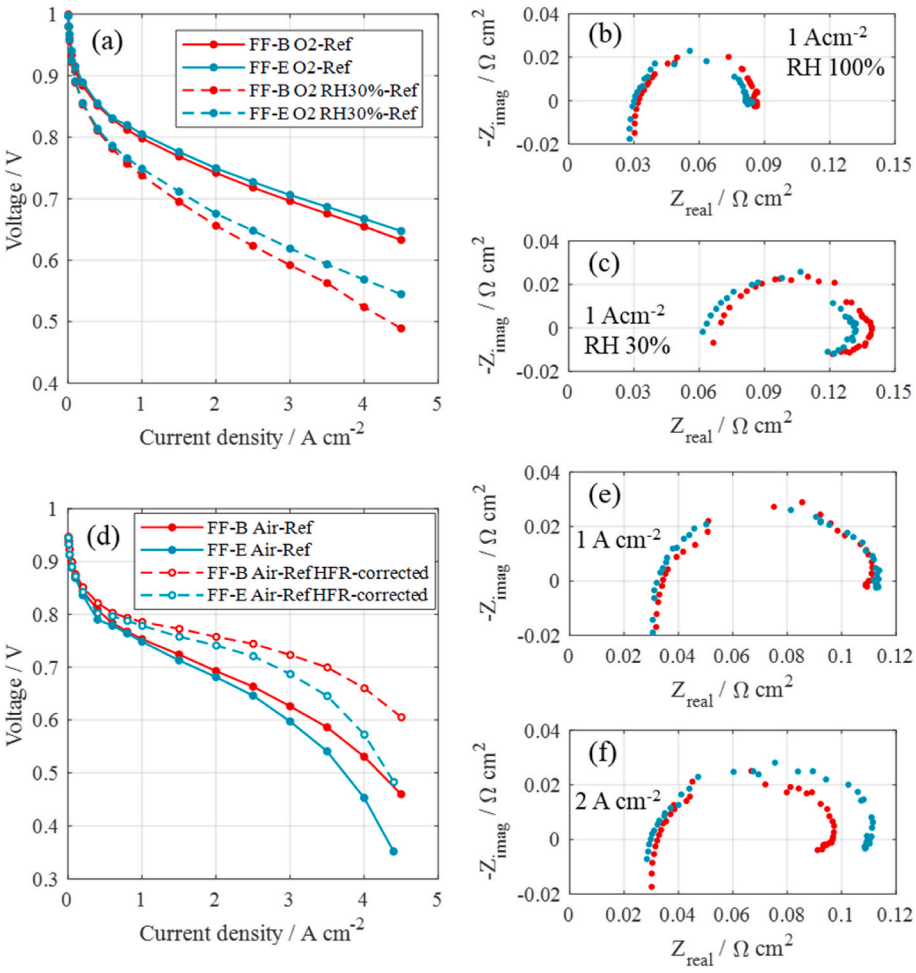

Fig. 11. Performance characterization of flow field plates with different channel depth (FF–B, FF-E). Pure oxygen/hydrogen conditions: (a) fully humidified (O2-Ref) and 30% relative humidity (O2 RH30%-Ref) polarization curves, (b) EIS at 1 A cm^{-2} under fully humified conditions (O2-Ref), (c) EIS at 1 A cm^{-2} at 30% relative humidity (O2 RH30%-Ref). Air/hydrogen fully humidified conditions (Air-Ref): (d) polarization curves and HFR-corrected polarization curves, (e) EIS at 1 A cm^{-2}, (f) EIS at 2 A cm^{-2}.

depicted in Fig. 11b and Fig. 11c respectively. The results highlight that the main distinction between the analysed flow field geometries is associated to the values of HFR. FF-E exhibits lower HFR compared to FF-B and this difference is more pronounced at low RH conditions. The observed outcomes are in accordance with the deeper cathode channels of FF-E, which results in a lower gas velocity and thus in an increased water retention [22,67]. This phenomenon is particularly notable at low RH gas reactants, where the increased water retention significantly enhances membrane hydration and consequently increases ion conductivity [68], leading to the differences in results observed in Fig. 11a.

Polarization curves performed in air/hydrogen under fully humidified conditions (Air-Ref) are reported in Fig. 11d. The flow field FF-E,

characterized by higher channel depth, results to be disadvantaged under these operating conditions. Indeed, FF-E exhibits lower performance compared to FF-B and this performance difference increases from low to high current density. Additionally, Fig. 11d also depicts the curves performed in air/hydrogen conditions with a voltage correction for the values of HFR obtained at 1 A cm^{-2}. Despite this correction, corrected and non-corrected curves presents the same trend, this suggests that the differences in performance of the two flow fields cannot be solely attributed to variations in HFR. EIS measurements with fully humidified air/hydrogen gas reactants (Air-Ref) performed at 1 A cm^{-2} and 2 A cm^{-2} are reported in Fig. 11e and Fig. 11f respectively. While comparable results are reached by the two samples at low current density, at 2 A cm^{-2} the flow flied characterized by deeper cathode channels shows an increase in the low-frequency arc confirming the previous findings which attribute the performance difference to a higher oxygen transport resistance due to lower gas velocity [24].

The experimental characterization points out the impact of cathode channel depth on performance and emphasises the effect of various phenomena under different operating conditions. Both water retention and oxygen transport resistance play a key role in flow field design, therefore the optimization of channel depth is essential to effectively address these considerations.

3.5. Oxygen transport resistance and high frequency resistance analysis

The oxygen transport resistance, derived from limiting current measurements, is reported in Fig. 12a as a function of the cathode gas pressure. Comparing FF-B and FF-E, which differ only in cathode channel depth, it is evident that this geometric parameter primarily affects the slope of the reported curves. The slope corresponds to the pressure-dependent component of the transport resistance, as described in section 2.3, which is related to intermolecular gas diffusion [69]. In accordance with the results of section 3.4, an increase in cathode channel depth leads to an increase in the transport resistance component [24]. This effect is caused by the reduction in gas velocity within the cathode channels, resulting from the increased cross sectional area, with the consequential reduction of oxygen transport [18]. Indeed, a variation in gas flow velocity within the channel affects the thickness of the laminar boundary layer, influencing velocity and mass transport convection through the GDL and subsequently impacting oxygen transport from the channel to the catalyst active sites. It is worth noting that similar outcomes are achieved by FF-A and FF-B, which are characterized by the same value of rib-to-channel thickness ratio. On the other hand, the increase of this ratio (FF–C and FF-D) return higher values for both pressure-dependent and pressure-independent components. The increase in rib-to-channel thickness ratio corresponds to a greater portion of the GDL covered by the ribs, resulting in an increased diffusion length for oxygen molecules to the catalyst layer, thus rising the transport resistance [70]. This trend is consistent with the findings from section 3.3, where increased mass transport loss is observed for flow fields with higher rib-to-channel thickness ratios.

The value of rib-to-channel thickness ratio also affects the high frequency resistance, as it is directly related to the contact area between the bipolar plate and the GDL [36]. The HFR values obtained at 1 A cm^{-2} under O2-Ref and O2 RH30%-Ref conditions are reported in Fig. 12b, in both operating conditions the HFR decreases from FF-A and FF-B to FF-C and FF-D. These differences are consistent with the observations described in section 3.3, where the impact of the contact area between the bipolar plate and the GDL on ohmic loss under various operating conditions is discussed [37]. FF-E, despite having a rib-to-channel thickness ratio comparable to flow fields FF-A and FF-B, exhibits HFR values in Fig. 12b that deviate from the trend observed in other samples. HFR values for FF-E are lower compared to other flow fields with similar rib-to-channel thickness ratio and this difference increases at low RH. This behaviour is attributed to the different cross sectional area, which is 2.5 times larger in FF-E compared to FF-B, this results in lower gas velocity and higher water retention in FF-E [21]. The increased water content improves ionomer hydration and reduces the HFR value, effect particularly evident under low RH conditions [71].

The geometric parameters of the cathode flow fields have shown to significantly influence transport resistance and electrical conductivity, crucial features affecting fuel cell stack performance [72]. Therefore, the development of variable flow field geometry, optimized for the local operating conditions occurring within the fuel cell stack, is of prime importance.

4. Conclusions

This study focuses on characterizing the performance of graphite-based flow fields on the cathode side of PEMFCs, featuring straight-parallel channels with varying geometric parameters. To reproduce real-world operations, boundary conditions for low power and high power operating modes were defined. A 1+1D PEMFC model was employed to assess local operating conditions across different regions within the fuel cell stack. These conditions obtained through the model were then experimentally reproduced using a zero-gradient hardware, developed on purpose to investigate flow field performance in small-scale configuration under uniform operating conditions.

The experimental campaign conducted under both LP and HP conditions reveals the primary limiting phenomena occurring at various

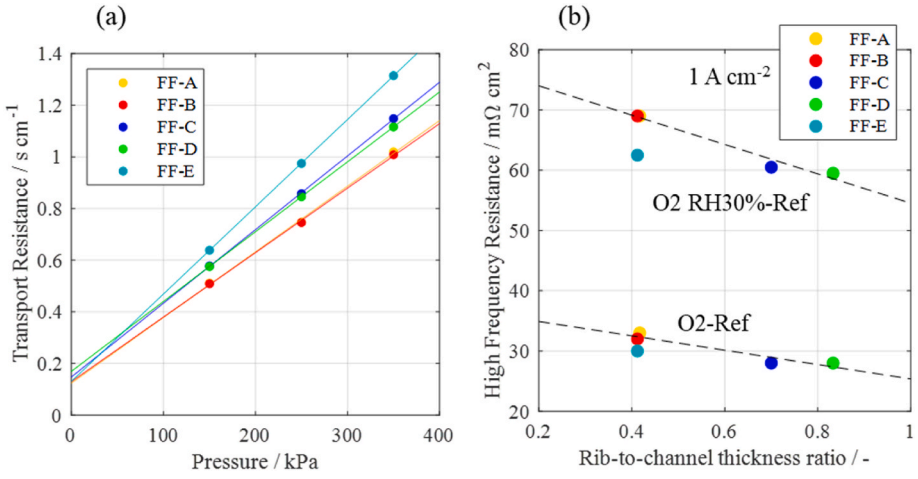

Fig. 12. (a) Oxygen transport resistance as function of the cathode gas pressure and (b) high frequency resistance evaluated under O2-Ref and O2 RH30%-Ref conditions at 1 A cm^{-2} of flow field plates characterized by different geometry.

positions along the channel under real-world operating conditions. Performance under LP conditions, investigated across a voltage range of 0.7 V–0.8 V, exhibits a bell-shaped power density profile, with a peak around 50% of the cathode channel length. This profile results from the combination of low cathode gas RH at the air inlet, leading to performance reduction due to low membrane hydration, and performance reduction at the air outlet region caused by high mass transport resistance. Under HP conditions, examined within a voltage range of 0.6 V–0.7 V, the power density profile initially increases due to gradual sample hydration, followed by a progressive reduction in performance towards the air outlet region driven by mass transport loss. Because of the lower operating voltage values of HP compared to LP conditions, the power density curve peak shifts towards a position closer to the air inlet compared to that observed under LP conditions.

The assessment of rib and channel features revealed their significant impact on performance. The rib-to-channel thickness ratio, which correlates with the contact surface between the bipolar plate and the GDL, directly affects electrical resistance. It has been demonstrated that performance at the air inlet region is primarily limited by ohmic loss, under these conditions an increase in the rib-to-channel thickness ratio results in higher performance obtained through a reduction in HFR. Results obtained at the air inlet demonstrate that a 1.7-fold increase in R/C from FF-B to FF-C leads to a performance enhancement of 10% under LP conditions and 17% under HP conditions.

Oxygen transport resistance becomes the primary limiting factor moving towards the air outlet region. Experimental results indicate that rib thickness significantly affects mass transport properties, a thicker rib leads to increased water accumulation in the GDL region under the rib. This water accumulation is crucial at the air inlet region under low RH conditions, where EIS measurements have demonstrated better MEA hydration, and it also impacts the middle and air outlet regions, where water accumulation may cause flooding phenomena.

Channel depth directly impacts gas velocity within the channels, thereby influencing transport properties. A greater channel depth corresponds to an increased cross sectional area, resulting in reduced gas velocity and, as evidenced by limiting current measurements, increased oxygen transport resistance. Moreover, the lower gas velocity leads to higher water retention, as observed by the reduced values of HFR under low RH conditions. The limitations in oxygen transport and the increased water retention lead to reduced performance in the air outlet region, where low oxygen mole fraction and flooding phenomena are the primary limiting factors. On the other hand, deeper channels enhance membrane hydration, addressing issues related to low ion conductivity, in particular in the air inlet and middle regions where performance is limited by ohmic loss. At the air inlet, the 2.5-fold increase in channel depth from FF-B to FF-E results in a performance improvement of 16% under LP conditions and of 12% under HP conditions.

The originality of the proposed methodology allows to provide detailed information on the local operation of a large-area bipolar plate using a small-area sample and a simple experimental setup. Furthermore, the novelty of the presented experimental analysis demonstrates the effect of rib and channel geometrical parameters on real-world operation of a PEMFC, contributing to the development of advanced high-performance flow field geometries. This novel approach allows for flow field optimization by reproducing the real-world conditions occurring locally in a full-scale cell within a small-scale configuration, eliminating the need for full-scale hardware and significantly reducing the cost and complexity of the testing setup. Moreover, the proposed methodology enables the isolation of the impact of each flow field geometric parameter variation on performance, leading to a deeper understanding of the limiting phenomena which cannot be achieved with full-scale samples.

The proposed methodology is highly adaptable and can be applied to a variety of research areas. For instance, it can be used in future studies to assess the impact of GDL characteristics on fuel cell performance by following the same procedures outlined in this paper. Additionally, degradation mechanisms can be investigated by reproducing the local degradation occurring in different regions of a fuel cell stack within a small-scale configuration, allowing for the isolation of driving factors affecting durability under controlled operating conditions that reproduce real-world operations. This research offers significant benefits for industrial applications by providing a simplified and cost-effective alternative to full-scale samples, enabling the investigation of local performance achievements across various positions along the channel.

CRediT authorship contribution statement

Delio Casadei: Writing – original draft, Visualization, Validation, Methodology, Investigation, Formal analysis, Data curation, Conceptualization. **Francesco Verducci:** Writing – review & editing, Investigation. **Amedeo Grimaldi:** Writing – review & editing. **Diego Croci:** Conceptualization. **Alessandro Palmieri:** Conceptualization. **Roberto Bianchi:** Conceptualization. **Gianmario Picciotti:** Supervision, Project administration. **Andrea Casalegno:** Supervision, Project administration, Methodology. **Andrea Baricci:** Writing – review & editing, Supervision, Methodology, Conceptualization.

Declaration of competing interest

The authors declare that they have no known competing financial interests or personal relationships that could have appeared to influence the work reported in this paper.

References

[1] Thai C, Brouwer J. Decarbonizing a solar PV and gas turbine microgrid with hydrogen and batteries. Energy Convers Manag 2023;292:117391. https://doi.org/10.1016/j.enconman.2023.117391.
[2] Ozturk M, Dincer I. A comprehensive review on power-to-gas with hydrogen options for cleaner applications. Int J Hydrogen Energy 2021;46:31511–22. https://doi.org/10.1016/j.ijhydene.2021.07.066.
[3] Pramuanjaroenkij A, Kakaç S. The fuel cell electric vehicles: the highlight review. Int J Hydrogen Energy 2023;48:9401–25. https://doi.org/10.1016/j.ijhydene.2022.11.103.
[4] Kampker A, Ayvaz P, Schön C, Karstedt J, Förstmann R, Welker F. Challenges towards large-scale fuel cell production: results of an expert assessment study. Int J Hydrogen Energy 2020;45:29288–96. https://doi.org/10.1016/j.ijhydene.2020.07.180.
[5] Cullen DA, Neyerlin KC, Ahluwalia RK, Mukundan R, More KL, Borup RL, et al. New roads and challenges for fuel cells in heavy-duty transportation. Nat Energy 2021;6:462–74. https://doi.org/10.1038/s41560-021-00775-z.
[6] Xiong K, Wu W, Wang S, Zhang L. Modeling, design, materials and fabrication of bipolar plates for proton exchange membrane fuel cell: a review. Appl Energy 2021;301:117443. https://doi.org/10.1016/j.apenergy.2021.117443.
[7] Kleen G, Gibbons W, Fornaciari J. Heavy-duty fuel cell system cost – 2022. DOE Hydrogen Program Record 2023:1–11.
[8] Wu CW, Zhang W, Han X, Zhang YX, Ma GJ. A systematic review for structure optimization and clamping load design of large proton exchange membrane fuel cell stack. J Power Sources 2020;476. https://doi.org/10.1016/j.jpowsour.2020.228724.
[9] Konno N, Mizuno S, Nakaji H, Ishikawa Y. Development of compact and high-performance fuel cell stack. SAE Int J Altern Powertrains 2015;4:123–9. https://doi.org/10.4271/2015-01-1175.
[10] Wu S, Yang W, Yan H, Zuo X, Cao Z, Li H, et al. A review of modified metal bipolar plates for proton exchange membrane fuel cells. Int J Hydrogen Energy 2021;46:8672–701. https://doi.org/10.1016/j.ijhydene.2020.12.074.
[11] Song Y, Zhang C, Ling CY, Han M, Yong RY, Sun D, et al. Review on current research of materials, fabrication and application for bipolar plate in proton exchange membrane fuel cell. Int J Hydrogen Energy 2020;45:29832–47. https://doi.org/10.1016/j.ijhydene.2019.07.231.
[12] Bi F, Yi P, Zhou T, Peng L, Lai X. Effects of Al incorporation on the interfacial conductivity and corrosion resistance of CrN film on SS316L as bipolar plates for proton exchange membrane fuel cells. Int J Hydrogen Energy 2015;40:9790–802. https://doi.org/10.1016/j.ijhydene.2015.06.012.
[13] Wilberforce T, Ijaodola O, Ogungbemi E, Khatib FN, Leslie T, El-Hassan Z, et al. Technical evaluation of proton exchange membrane (PEM) fuel cell performance – a review of the effects of bipolar plates coating. Renew Sustain Energy Rev 2019;113:109286. https://doi.org/10.1016/j.rser.2019.109286.
[14] Gao X, Chen J, Xu R, Zhen Z, Zeng X, Chen X, et al. Research progress and prospect of the materials of bipolar plates for proton exchange membrane fuel cells (PEMFCs). Int J Hydrogen Energy 2024;50:711–43. https://doi.org/10.1016/j.ijhydene.2023.09.005.

[15] Thapa S, Ganesh V, Agarwal H, Sahu AK. Performance evaluation of cathode channels with different cross-sections for open-cathode polymer electrolyte membrane fuel cell stack. J Power Sources 2024;603:234398. https://doi.org/10.1016/j.jpowsour.2024.234398.
[16] Wang XR, Ma Y, Gao J, Li T, Jiang GZ, Sun ZY. Review on water management methods for proton exchange membrane fuel cells. Int J Hydrogen Energy 2021;46:12206–29. https://doi.org/10.1016/j.ijhydene.2020.06.211.
[17] Benkovic D, Fink C, Iranzo A. Qualitative and quantitative determination of liquid water distribution in a PEM fuel cell. Int J Hydrogen Energy 2024;52:1360–70. https://doi.org/10.1016/j.ijhydene.2023.09.161.
[18] Gwak G, Lee J, Ghasemi M, Choi J, Lee SW, Jang SS, et al. Analyzing oxygen transport resistance and Pt particle growth effect in the cathode catalyst layer of polymer electrolyte fuel cells. Int J Hydrogen Energy 2020;45:13414–27. https://doi.org/10.1016/j.ijhydene.2020.03.080.
[19] Ding Q, Zhu KQ, Xu JH, Zhang BX, Yang YR, Yang C, et al. Evaluation criterion of flow fields in PEM fuel cells based on entropy generation analysis. Int J Hydrogen Energy 2023;48:2328–40. https://doi.org/10.1016/j.ijhydene.2022.10.112.
[20] Colombo E, Baricci A, Bisello A, Guetaz L, Casalegno A. PEMFC performance decay during real-world automotive operation: evincing degradation mechanisms and heterogeneity of ageing. J Power Sources 2023;553:232246. https://doi.org/10.1016/j.jpowsour.2022.232246.
[21] Limjeerajarus N, Charoen-Amornkitt P. Effect of different flow field designs and number of channels on performance of a small PEFC. Int J Hydrogen Energy 2015;40:7144–58. https://doi.org/10.1016/j.ijhydene.2015.04.007.
[22] Choi KS, Kim HM, Moon SM. Numerical studies on the geometrical characterization of serpentine flow-field for efficient PEMFC. Int J Hydrogen Energy 2011;36:1613–27. https://doi.org/10.1016/j.ijhydene.2010.10.073.
[23] Shimpalee S, Greenway S, Van Zee JW. The impact of channel path length on PEMFC flow-field design. J Power Sources 2006;160:398–406. https://doi.org/10.1016/j.jpowsour.2006.01.099.
[24] Zhang Z, Bai F, He P, Li Z, Tao WQ. A novel cathode flow field for PEMFC and its performance analysis. Int J Hydrogen Energy 2023;48:24459–80. https://doi.org/10.1016/j.ijhydene.2023.03.130.
[25] Ahmed DH, Sung HJ. Effects of channel geometrical configuration and shoulder width on PEMFC performance at high current density. J Power Sources 2006;162:327–39. https://doi.org/10.1016/j.jpowsour.2006.06.083.
[26] Shimpalee S, Van Zee JW. Numerical studies on rib & channel dimension of flow-field on PEMFC performance. Int J Hydrogen Energy 2007;32:842–56.
[27] Rahimi-Esbo M, Ranjbar AA, Ramiar A, Alizadeh E, Aghaee M. Improving PEM fuel cell performance and effective water removal by using a novel gas flow field. Int J Hydrogen Energy 2016;41:3023–37. https://doi.org/10.1016/j.ijhydene.2015.11.001.
[28] Kim J, Luo G, Wang CY. Modeling two-phase flow in three-dimensional complex flow-fields of proton exchange membrane fuel cells. J Power Sources 2017;365:419–29.
[29] Yin Y, Wang X, Shangguan X, Zhang J, Qin Y. Numerical investigation on the characteristics of mass transport and performance of PEMFC with baffle plates installed in the flow channel. Int J Hydrogen Energy 2018;43:8048–62. https://doi.org/10.1016/j.ijhydene.2018.03.037.
[30] Afshari E, Mosharaf-Dehkordi M, Rajabian H. An investigation of the PEM fuel cells performance with partially restricted cathode flow channels and metal foam as a flow distributor. Energy 2017;118:705–15. https://doi.org/10.1016/j.energy.2016.10.101.
[31] Perng SW, Wu HW. A three-dimensional numerical investigation of trapezoid baffles effect on non-isothermal reactant transport and cell net power in a PEMFC. Appl Energy 2015;143:81–95. https://doi.org/10.1016/j.apenergy.2014.12.059.
[32] Cai Y, Wu D, Sun J, Chen B. The effect of cathode channel blockages on the enhanced mass transfer and performance of PEMFC. Energy 2021;222. https://doi.org/10.1016/j.energy.2021.119951.
[33] Liao S, Qiu D, Yi P, Peng L, Lai X. Modeling of a novel cathode flow field design with optimized sub-channels to improve drainage for proton exchange membrane fuel cells. Energy 2022;261:125235.
[34] Iranzo A, Muñoz M, López E, Pino J, Rosa F. Experimental fuel cell performance analysis under different operating conditions and bipolar plate designs. Int J Hydrogen Energy 2010;35:11437–47. https://doi.org/10.1016/j.ijhydene.2010.05.056.
[35] Micoud F. 3.1 Innovative cell design features to improve PEMFC performancese. 1st Public Work DOLPHIN Proj 2021. https://www.dolphin-fc.eu/fileadmin/user_upload/3_1_DOLPHIN_Workshop1_Innovative_features.pdf.
[36] Qiu D, Janßen H, Peng L, Irmscher P, Lai X, Lehnert W. Electrical resistance and microstructure of typical gas diffusion layers for proton exchange membrane fuel cell under compression. Appl Energy 2018;231:127–37. https://doi.org/10.1016/j.apenergy.2018.09.117.
[37] Qiu D, Peng L, Yi P, Lai X. A micro contact model for electrical contact resistance prediction between roughness surface and carbon fiber paper. Int J Mech Sci 2017;124–125:37–47. https://doi.org/10.1016/j.ijmecsci.2017.02.026.
[38] Edwards H, Pereira MP, Gharaie S, Omrani R, Shabani B. Computational fluid dynamics modelling of proton exchange membrane fuel cells: accuracy and time efficiency. Int J Hydrogen Energy 2024;50:682–710. https://doi.org/10.1016/j.ijhydene.2023.09.004.
[39] Baricci A, Mereu R, Messaggi M, Zago M, Inzoli F, Casalegno A. Application of computational fluid dynamics to the analysis of geometrical features in PEM fuel cells flow fields with the aid of impedance spectroscopy. Appl Energy 2017;205:670–82. https://doi.org/10.1016/j.apenergy.2017.08.017.
[40] Zhang Y, He S, Jiang X, Xiong M, Ye Y, Yang X. Three-dimensional multi-phase simulation of different flow fields with cooling channel in proton exchange membrane fuel cell. Int J Hydrogen Energy 2022;47:37929–44. https://doi.org/10.1016/j.ijhydene.2022.08.286.
[41] von Tettau P, Sterlepper S, Mauermann P, Wick M, Tinz S, Jesser M, et al. Laboratory assessments applied to mass-produced automotive fuel cells. Int J Hydrogen Energy 2024;52:1127–36. https://doi.org/10.1016/j.ijhydene.2023.10.309.
[42] Colombo E, Casadei D, Baricci A, Casalegno A. An open-source zero-gradient cell hardware to improve and accelerate durability testing of PEM fuel cells. HardwareX 2023;16:e00495. https://doi.org/10.1016/j.ohx.2023.e00495.
[43] Verducci F, Grimaldi A, Colombo E, Casalegno A, Baricci A. Dynamic modeling of polymer electrolyte membrane fuel cells under real-world automotive driving cycle with experimental validation on segmented single cell. Renew Energy 2024;234:121194. https://doi.org/10.1016/j.renene.2024.121194.
[44] Wood DL, Borup RL. Estimation of mass-transport overpotentials during long-term PEMFC operation. J Electrochem Soc 2010;157:B1251. https://doi.org/10.1149/1.3454740.
[45] Colombo E, Baricci A, Mora D, Guetaz L, Casalegno A. An innovative accelerated stress test representative of automotive PEMFC degradation mechanisms validated on 1000 hours real-world operation. J Power Sources 2023;580:233376. https://doi.org/10.1016/j.jpowsour.2023.233376.
[46] Baker DR, Caulk DA, Neyerlin KC, Murphy MW. Measurement of oxygen transport resistance in PEM fuel cells by limiting current methods. J Electrochem Soc 2009;156:B991.
[47] Greszler TA, Caulk D, Sinha P. The impact of platinum loading on oxygen transport resistance. J Electrochem Soc 2012;159:F831–40.
[48] Nonoyama N, Okazaki S, Weber AZ, Ikogi Y, Yoshida T. Analysis of oxygen-transport diffusion resistance in proton-exchange-membrane fuel cells. J Electrochem Soc 2011;158:B416–23.
[49] Sellin RC, Mozet K, Ménage A, Dillet J, Didierjean S, Maranzana G. Measuring electro-osmotic drag coefficients in PFSA membranes without any diffusion assumption. Int J Hydrogen Energy 2019;44:24905–12. https://doi.org/10.1016/j.ijhydene.2019.07.076.
[50] Xu S, Liao P, Yang D, Li Z, Li B, Ming P, et al. Liquid water transport in gas flow channels of PEMFCs: a review on numerical simulations and visualization experiments. Int J Hydrogen Energy 2023;48:10118–43. https://doi.org/10.1016/j.ijhydene.2022.12.140.
[51] Weber AZ, Borup RL, Darling RM, Das PK, Dursch TJ, Gu W, et al. A critical review of modeling transport phenomena in polymer-electrolyte fuel cells. J Electrochem Soc 2014;161:F1254–99. https://doi.org/10.1149/2.0751412jes.
[52] Rezaei Niya SM, Phillips RK, Hoorfar M. Process modeling of the impedance characteristics of proton exchange membrane fuel cells. Electrochim Acta 2016;191:594–605. https://doi.org/10.1016/j.electacta.2016.01.128.
[53] Tang Z, Huang QA, Wang YJ, Zhang F, Li W, Li A, et al. Recent progress in the use of electrochemical impedance spectroscopy for the measurement, monitoring, diagnosis and optimization of proton exchange membrane fuel cell performance. J Power Sources 2020;468:228361. https://doi.org/10.1016/j.jpowsour.2020.228361.
[54] Owejan JP, Trabold TA, Mench MM. Oxygen transport resistance correlated to liquid water saturation in the gas diffusion layer of PEM fuel cells. Int J Heat Mass Tran 2014;71:585–92. https://doi.org/10.1016/j.ijheatmasstransfer.2013.12.059.
[55] Kahraman H, Orhan MF. Flow field bipolar plates in a proton exchange membrane fuel cell: analysis & modeling. Energy Convers Manag 2017;133:363–84. https://doi.org/10.1016/j.enconman.2016.10.053.
[56] Grimaldi A, Baricci A, De Antonellis S, Oldani C, Casalegno A. Experimental study and modeling of water transport through short-side-chain perfluorosulfonic acid membranes. J Power Sources 2023;558:232556. https://doi.org/10.1016/j.jpowsour.2022.232556.
[57] Zhang H, Rahman MA, Mojica F, Sui PC, Chuang PA. A comprehensive two-phase proton exchange membrane fuel cell model coupled with anisotropic properties and mechanical deformation of the gas diffusion layer. Electrochim Acta 2021;382:138273. https://doi.org/10.1016/j.electacta.2021.138273.
[58] Liu S, Yuan S, Liang Y, Li H, Xu Z, Xu Q, et al. Engineering the catalyst layers towards enhanced local oxygen transport of Low-Pt proton exchange membrane fuel cells: materials, designs, and methods. Int J Hydrogen Energy 2023;48:4389–417. https://doi.org/10.1016/j.ijhydene.2022.10.249.
[59] Nascimento AL, Yahyaoui I, Fardin JF, Encarnação LF, Tadeo F. Modeling and experimental validation of a PEM fuel cell in steady and transient regimes using PSCAD/EMTDC software. Int J Hydrogen Energy 2020;45:30870–81. https://doi.org/10.1016/j.ijhydene.2020.04.184.
[60] Baricci A, Bisello A, Serov A, Odgaard M, Atanassov P, Casalegno A. Analysis of the effect of catalyst layer thickness on the performance and durability of platinum group metal-free catalysts for polymer electrolyte membrane fuel cells. Sustain Energy Fuels 2019;3:3375–86. https://doi.org/10.1039/c9se00252a.
[61] Ouaidat G, Cherouat A, Kouta R, Chamoret D. Numerical modeling of the mechanical behavior of proton exchange membrane fuel cell performance: design of experiment study and optimization. Int J Hydrogen Energy 2020;45:25210–26. https://doi.org/10.1016/j.ijhydene.2020.06.015.
[62] Afrasiab H, Davoodi KH, Barzegari MM, Gholami M, Hassani A. A novel constitutive stress-strain law for compressive deformation of the gas diffusion layer. Int J Hydrogen Energy 2022;47:32167–80. https://doi.org/10.1016/j.ijhydene.2022.07.127.
[63] Manso AP, Marzo FF, Barranco J, Garikano X, Garmendia Mujika M. Influence of geometric parameters of the flow fields on the performance of a PEM fuel cell. A review. Int J Hydrogen Energy 2012;37:15256–87. https://doi.org/10.1016/j.ijhydene.2012.07.076.

[64] Bao Z, Niu Z, Jiao K. Analysis of single- and two-phase flow characteristics of 3-D fine mesh flow field of proton exchange membrane fuel cells. J Power Sources 2019;438:226995. https://doi.org/10.1016/j.jpowsour.2019.226995.
[65] Qiu D, Peng L, Yi P, Lehnert W, Lai X. Review on proton exchange membrane fuel cell stack assembly: quality evaluation, assembly method, contact behavior and process design. Renew Sustain Energy Rev 2021;152:111660. https://doi.org/10.1016/j.rser.2021.111660.
[66] Wang Y, Wang X, Fan Y, He W, Guan J, Wang X. Numerical investigation of tapered flow field configurations for enhanced polymer electrolyte membrane fuel cell performance. Appl Energy 2022;306:118021. https://doi.org/10.1016/j.apenergy.2021.118021.
[67] Kim J, Luo G, Wang CY. Modeling liquid water re-distributions in bi-porous layer flow-fields of proton exchange membrane fuel cells. J Power Sources 2018;400:284–95. https://doi.org/10.1016/j.jpowsour.2018.08.018.
[68] Pan M, Pan C, Li C, Zhao J. A review of membranes in proton exchange membrane fuel cells: transport phenomena, performance and durability. Renew Sustain Energy Rev 2021;141:110771. https://doi.org/10.1016/j.rser.2021.110771.
[69] Simon C, Hasché F, Gasteiger HA. Influence of the gas diffusion layer compression on the oxygen transport in PEM fuel cells at high water saturation levels. J Electrochem Soc 2017;164:F591–9. https://doi.org/10.1149/2.0691706jes.
[70] Chowdhury A, Radke CJ, Weber AZ. Transport resistances in fuel-cell catalyst layers. ECS Meet Abstr 2017:1391. https://doi.org/10.1149/ma2017-02/32/1391. MA2017-02.
[71] Liu Q, Lan F, Chen J, Zeng C, Wang J. A review of proton exchange membrane fuel cell water management: membrane electrode assembly. J Power Sources 2022;517:230723. https://doi.org/10.1016/j.jpowsour.2021.230723.
[72] Jiao K, Xuan J, Du Q, Bao Z, Xie B, Wang B, et al. Designing the next generation of proton-exchange membrane fuel cells. Nature 2021;595:361–9. https://doi.org/10.1038/s41586-021-03482-7.